The Sensitive Gas-Sensing by Creating Adsorption Active Sites: Coating an SnO_2 Layer on Triangle Arrays

*Shipu Xu, Yang Xu, Huaping Zhao, Rui Xu, and Yong Lei**

Institute für Physik & IMN MacroNano (ZIK), Technische Universität Ilmenau, Ilmenau 98693, Germany

KEYWORDS: gas sensors, surface adsorption, triangle arrays, SnO_2, Kelvin force microscopy

ABSTRACT: It is a widely used strategy to enhance a gas sensor sensitivity by improving its surface area, but this process, including bonding the sensing block into a device substrate, needs complex manipulations. This work shows a concept of adsorption active site, by which an SnO_2 layer (6.85 nm thin) is directly coated on a triangle array substrate to be of an ensemble of triangular convex adsorption active sites (TCAASs). The resultant SnO_2 gas sensors, with TCAAS periods ranging from 289 to 1154 nm, exhibit an adsorption-active-site-dependent sensitivity and present a low detection limit of around 6 ppm ethanol gas at room temperature. By characterizations of Kelvin force microscopy, a large surface potential variation exists on these adsorption active sites after introducing ethanol gas, distinctly showing a local adsorption enhancement. These results confirm that the creation of adsorption active sites can efficiently increase surface adsorption of a sensor to realize its sensitive gas-sensing.

1. INTRODUCTION

Sensing gaseous molecules is important to environmental monitoring, control of chemical process, and agriculture applications.[1-8] Among them, sensitive gas-sensing is always a constant pursuit. To this end, improving the surface area of a gas sensor is a widely used strategy,[1,3-6] however, of which process, including bonding the sensing block into a device substrate, needs complex manipulations. It is worthy to explore an efficient approach to prepare a gas sensor with high sensitivity.

Gas-sensing sensitivity is positively attributed to surface adsorption of the substrate. Tracing the origin of the surface adsorption and exploiting it in gas-sensing provide a high possibility to enhance the sensitivity of gas sensors. Thermodynamically, the surface adsorption is a spontaneous process accompanying with decreasing of Gibbs free energy ($\Delta G < 0$). In this decreasing of Gibbs free energy, there is a correlation between the changes in Gibbs free energy, entropy (S), and enthalpy (H):

$$\Delta G = \Delta H - T\Delta S \quad (1)$$

Adsorption confines a gaseous molecule to the substrate, which induces an unfavourable entropy change, $\Delta S < 0$. Thus, ΔH shall be negative (exothermic) for the gaseous molecules turned from the gas phase to the adsorbed phase ($H_a - H_g < 0$). A low enthalpy of the adsorbed phase (i.e., H_a) exists when a gaseous molecule is adsorbed on the substrate area with a lot of stepped and kinked crystal surfaces. Therefore, the substrate area rich of the stepped and kinked crystal surfaces should tend to adsorb more gaseous molecules than those on the other area. For example, in a gas-sensing work using three-dimensional (3D) pore arrays,[9] the structure of the 3D pore is divided into two adsorption areas: (i) pore wall and (ii) the convex along the surface pore. The pore convex is a

typical area with lots of stepped and kinked crystal surfaces.[10-13] As a result, this pore convex absorbs more gaseous molecules than those on the pore wall. Inspired by the high efficiency of the convex related to surface adsorption, it is worthy to create a gas sensor with a convex-rich morphology for realizing sensitive gas-sensing.

Triangle is of a convex-rich morphology and is already developed for sensing gaseous molecules.[14-17] By colloidal-monolayer-based method, triangles can be easily aligned into a regular array and further adjusted to achieve an optimized performance in sensing applications.[14,18-22] This adjustment includes changing the sensing volume by controlling the triangle nanoparticle size, period, and shape, for which we just need to vary the deposition parameters during the sample preparation: (i) the monolayer-nanosphere size and (ii) deposition time.[20-22] Considering such easy accessibility of the triangle array morphology related to the sensitive sensing, we herein coat a thin layer of SnO_2 on the triangle array substrate for an ensemble of triangular convex adsorption active sites (TCAASs), by which a surface adsorption enhancement of the SnO_2 layer can be realized for the sensitive gas-sensing.

As a proof of concept, by the colloidal-monolayer-based method, a series of triangle array substrates are prepared with different periods, ranging from 289 to 1154 nm. After coating an SnO_2 layer (6.85 nm thin), the resultant gas sensors are characterized by different sizes of the TCAASs. It is found that, these samples show a TCAAS-dependent sensitivity and present a low detection limit of around 6 ppm ethanol gas at room temperature. Comparably, without adsorption active sites, a flat SnO_2 layer has no gas-sensing responses even to a high concentration of ethanol gas (25 ppm). In the investigation of the gas-sensing mechanism, by Kelvin force microscopy (KFM), a local adsorption enhancement on the TCAAS is distinctly characterized by a large variation of surface potential after introducing ethanol gas. These results confirm that the creation of the

adsorption active site can efficiently enhance the surface adsorption of the gas sensors for their sensitive gas-sensing.

2. EXPERIMENTAL SECTION

2.1. Fabrication of a Colloidal Monolayer. Monodispersed polystyrene nanosphere suspensions (2.5 wt% in water, surfactant free) were bought from Alfa Aesar Company. An ordinary glass substrate (1.5 × 1.5 cm^2) was ultrasonically cleaned in acetone and then in ethanol for 1 hour. Subsequently, the substrate was mounted on a custom-built spin coater. An amount of 10 μL of the nanosphere suspension was dropped onto the substrate. A large-area colloidal monolayer (> 1 cm^2) was fabricated by a spin-coating method at a speed of 800 rotations per minute.

2.2. Fabrication of SnO_2 layers on Triangle Arrays. A colloidal monolayer was used as a deposition mask, through which a 10-nm-thick layer of titanium (Ti) was deposited by physical vapour deposition. The deposition rate was maintained at 0.02 Å/s, and the vacuum level was lower than 10E-6 Pa. After the deposition process, the colloidal monolayer was immersed into CH_2Cl_2 within 10 minutes for its removing. The generated Ti triangle array was then coated with a 6.85-nm-thick layer of SnO_2 by using a PicoSun SUNALE R-150 atomic layer deposition system (PicoSun, Finland), according to the following procedure which is different to the normal process of nanocomposite fabrications.[23,24] In this process, the reaction chamber was firstly heated to 250 °C, then $SnCl_4$ and H_2O were respectively chosen as the precursors of Sn and O. $SnCl_4$ was pulsed for 0.1 s and purged for 10 s, followed by a 0.1 s pulse and a 10 s purge of H_2O. This procedure was repeated 500 times, according to the growth rate of ~0.14 Å per cycle to reach a thickness of 6.85 nm. In this mean, colloidal monolayers with different diameters of nanospheres were used as a template, and SnO_2 layers on different triangle arrays can be obtained.

2.3. Characterizations of KFM. The sample was placed on the sample stage and was grounded. A platinum/silicon (Pt/Si) tip with 75 Hz of resonance was used. The scan rate was set at 1 Hz, and the scan area was 3.5 μm^2. The measurement system was conducted in a sealed box, by which different detected atmospheres were introduced and removed. The detected atmosphere was changed prior to the KFM acquaintances: (i) in air and (ii) with 25 ppm ethanol gas. The KFM measurement was performed by NTEGRA Spectra system.

2.4. Gas-Sensing Tests. The gas-sensing test were conducted in an air-tight chamber with electrical feedthroughs. A voltage of 4 V was applied to the device, and the variation of the output current was monitored and recorded with the changes in the gas environment using a Keithley semiconducting testing system. The reducing gas, 25 ppm ethanol, was chosen as a target gas. The gas-sensing measurement involves three sequential steps: (1) a base value of the output current from the sensor in air was recorded; (2) a calculated volume of detected gas was introduced into the chamber, and the signal on the variation of output current was simultaneously recorded; (3) After the signal stabilized, the chamber was opened to remove the detected gas, and the signal of the output current was simultaneously recorded until it reached a steady state. The *I-V* measurements were also conducted by this sensing system. Hall effect characterizations of the SnO_2 samples were conducted by Accent HL5500 measurement system.

2.5. Characterizations. The morphology of the samples on the device substrate were examined by scanning electron microscopy (SEM, S4800 Hitachi and Quanta 250 FEG) and atomic force microscopy (Dimension V Veeco-Bruker). The thickness of the SnO_2 layer was measured by the ellipsometry (SENTECH SE500). The compositions were characterized by X-ray diffraction (XRD, D/max2200, with Cu-Kα radiation) and X-ray photoelectron spectroscopy (XPS,

ESCALAB 250). Samples for the XRD and XPS measurements were prepared on the Si substrates under the same conditions as those prepared on the device substrate.

3. RESULTS AND DISCUSSION

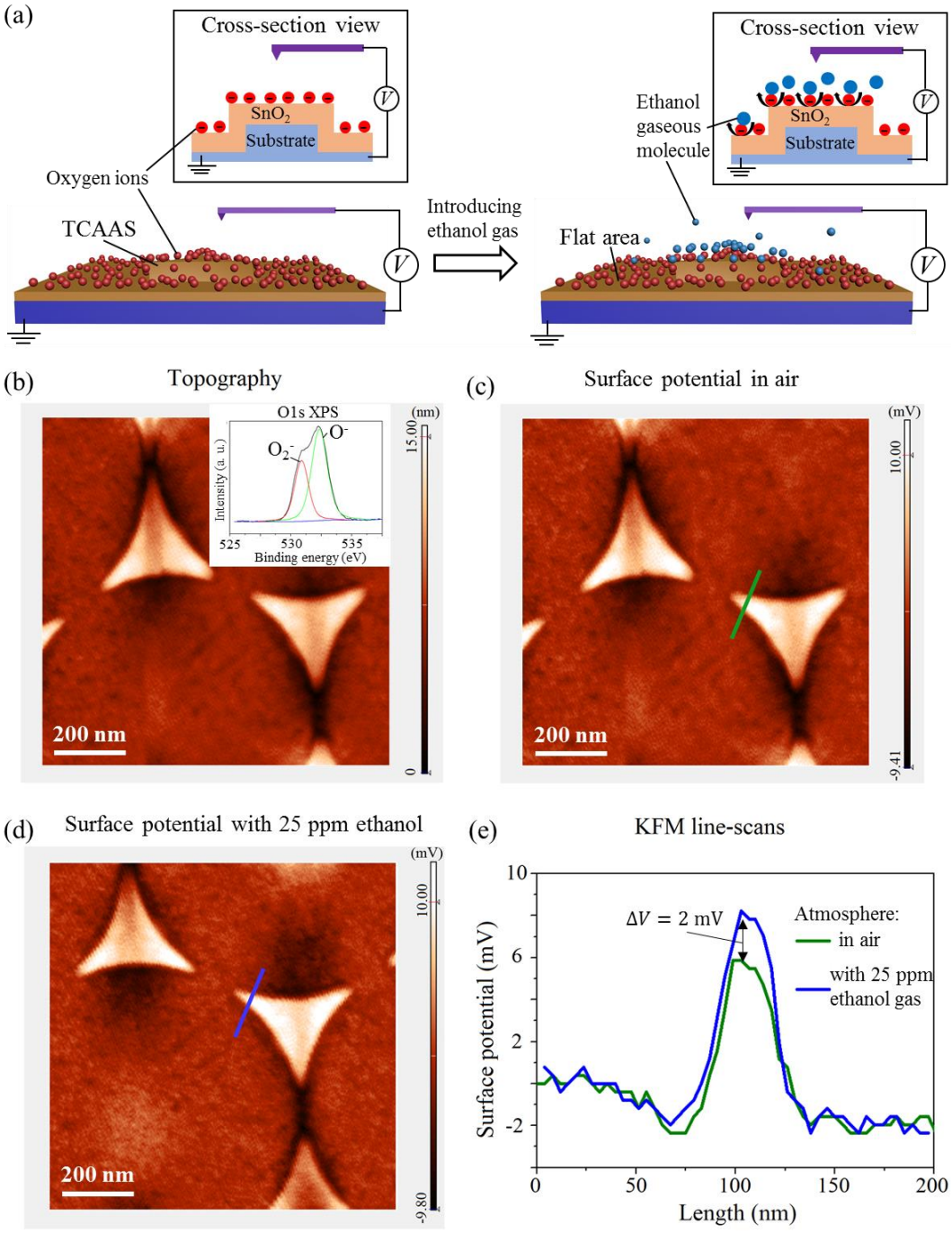

Figure 1. (a) Schematic representations showing the KFM setup for measuring the adsorption enhancement on the TCAAS, an SnO_2 layer on a substrate with the convex, from a tilted and a cross-section view (the insets in a). The TCAAS can adsorb more ethanol gaseous molecules to react with surficial oxygen ions than those of the flat area. (b-d) An Atomic force microscopy (AFM) image (b) and KFM images (c and d) from a same area of the sample, and the sample O1s XPS spectrum (the inset in b) showing surficial oxygen ions (O_2^- and O^-) with binding energy of 532.4 and 531.6 eV. Successive changes in atmospheres are made prior to each KFM image acquisition: (c) in air and (d) with 25 ppm ethanol. (e) Surface potentials of line-scans across the TCAAS in air and with 25 ppm ethanol.

3.1. Adsorption Enhancement on the Triangular Convex. Considering that the triangular convex is designed as an adsorption active site for enhancing surface adsorption, adsorption enhancement on the triangular convex shall be proved before the further ensemble of the triangles. To this end, we firstly investigate an adsorption behavior on the model material, i.e., SnO_2. In air, SnO_2 adsorbs atmospheric oxygen molecules (O_2), and a surficial reaction occurs, as shown by the following Equation 2:[25-27]

$$O_2 \xrightarrow{e^-} O_2^- \xrightarrow{e^-} 2O^- \qquad (2)$$

where adsorbed O_2 traps electrons from SnO_2. The resulting oxygen ions (O_2^- and O^-) with binding energies of 532.4 and 531.6 eV are demonstrated to exist on the SnO_2 surface by XPS (the inset in Figure 1b). These oxygen ions can carry negative surface potential on the SnO_2 surface.[28, 29] We introduce the ethanol gas to adjust the surface potential of the sample (see Supporting Information S1 for the existence of ethanol gaseous molecules on the sample surface), where the previously negative surface potential will turn positively via the following reaction, Equation 3:[30]

$$C_2H_5OH_{(g)} + \frac{1}{2}O^- + \frac{1}{4}O_2^- \rightarrow CH_3CHO_{(g)} + H_2O_{(g)} + \frac{3}{4}e^- \quad (3)$$

Based on this potential adjustment, we can characterize adsorption quantity on the TCAAS by its surface-potential variation.

It is anticipated that, a large surface-potential increase would occur on the TCAAS where more ethanol gaseous molecules were adsorbed than those on the flat area. In this regard, we use KFM, a well-accepted characterization for the surface potential,[31-33] to estimate a surface-potential increase on the TCAAS. Figure 1a schematically presents a KFM setup for measuring a surface-adsorption behavior on the TCAAS from a tilted and a cross-section view (the insets in Figure 1a), and the AFM image in Figure 1b shows that the TCAAS is formed by an SnO_2 layer coated on a convex substrate.

In a KFM scan, an alternating current (AC) voltage (V_{AC}) at frequency ω is added to the direct current (DC) voltage (V_{DC}) applied to the probe, and the voltage difference (ΔV_0) between the probe and the sample is presented by the following equation, Equation 4:

$$\Delta V_0 = V_{DC} - V_{PD} + V_{AC}\sin(\omega t) \quad (4)$$

where V_{PD} is a potential difference between the sample surface and the tip. The electrostatic force (F_{es}) between the tip and sample can thus be formulated as follow, Equation 5:

$$F_{es} = -\frac{1}{2}\frac{\partial C(z)}{\partial z}[V_{DC} - V_{PD} + V_{AC}\sin(\omega t)]^2 \quad (5)$$

where $\partial C(z)/\partial z$ is the gradient of the capacitance between the tip and the sample surface. From Equation 5, we can gain the following equation, Equation 6:[34]

$$F_{\omega} = -\frac{\partial C(z)}{\partial z}(V_{DC} - V_{PD})V_{AC}\sin(\omega t) \quad (6)$$

where F_{ω} with frequency ω is used to measure the V_{PD}. A lock-in amplifier is utilized to extract F_{ω}. As the output signal of the lock-in-amplifier is nullified and F_{ω} equals zero, the V_{PD} value can be measured by applying V_{DC} to the tip. Considering the sample is grounded, the value of V_{PD} is thus equal to the surface potential of the sample aroused by the adsorbed oxygen ions.

Based on the above mechanism of KFM, successive changes in atmospheres are made prior to each KFM image acquisition: (i) in air and (ii) with 25 ppm ethanol gas. Figure 1c and d respectively show surface potentials in air (Figure 1c) and with 25 ppm ethanol gas (Figure 1d). The corresponding potential profiles across a same selected area (Figure 1e) show that a distinct surface potential increase (ΔV = 2 mV) occurs on the TCAAS rather than the flat area, after introducing the ethanol gas. This comparison of surface-potential variations demonstrates a fact that the TCAAS can adsorb more ethanol gaseous molecules to react with the surficial oxygen ions, proving an adsorption enhancement on the TCAAS.

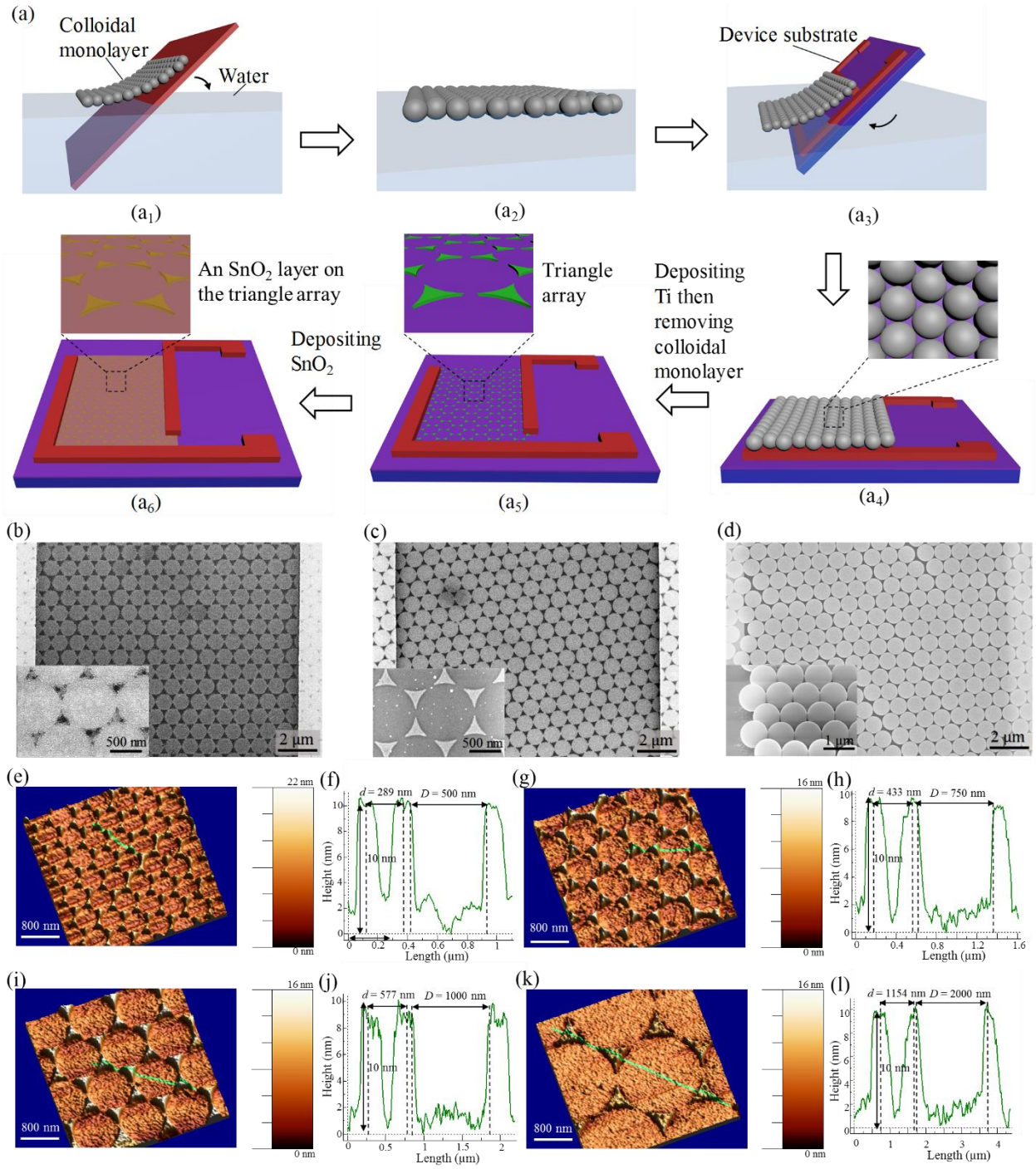

Figure 2. (a) Schematic representation of procedures for fabricating the sample: (a_1) transferring a colloidal monolayer to water; (a_2) the colloidal monolayer floated on the water; (a_3) picking up the colloidal monolayer with a device substrate; (a_4) the colloidal monolayer covering on the

device substrate (the inset in a_4 showing the magnified image of the colloidal monolayer); (a_5) a triangle array obtained by physical vapour deposition method after the removal of the colloidal monolayer (the inset in a_5 showing the magnified image of the array); (a_6) the SnO_2 layer on the array obtained after coating SnO_2 (the inset in a_6 showing the magnified image of the SnO_2 layer). (b-d) The SEM images showing plane views of the SnO_2 layer on the triangle array (b), the triangle array (c), and the colloidal monolayer (d, 1μm of the nanosphere diameter) between two contact electrodes. The insets in b and c showing the magnified images of the SnO_2 layer and the triangle array base. The inset in d showing a tilted view of the colloidal monolayer. (e-l) AFM images and their profiles across selected areas showing SnO_2 layers on triangle arrays with different values of *d*, such as 289 nm (e and f), 433 nm (g and h), 577 nm (i and j), and 1154 nm (k and l). *D* and *d* are the template nanosphere diameter and the inter-TCAAS spacing (i.e., the array period), respectively.

3.2. Gas Sensors Formed by Coating an SnO_2 Layer on Triangle Arrays. Inspired by the adsorption enhancement on the TCAAS, we coat a thin layer of SnO_2 on a triangle array for an ensemble of TCAASs. Fabrication process of the sample is described in Figure 2a. Firstly, a colloidal monolayer was transferred to water (Figure $2a_1$) and floated on the gas-liquid interface (Figure $2a_2$).[35] Next this floated colloidal monolayer was picked up with a device substrate (Figure $2a_3$). For the configuration of the device substrate, interdigitated Pt/Ti electrodes were seated on a substrate, a p-type Si substrate capped with a 300-nm-thick oxide layer. After being dried up at room temperature for a day, the colloidal monolayer covered on the device substrate surface (Figure $2a_4$). This colloidal monolayer contains triangular voice spaces created by three neighboring nanospheres (the magnified image in Figure $2a_4$). A 10-nm-thick layer of Ti was then deposited over the colloidal-monolayer-coated substrate. In a lift-off step, the colloidal monolayer

was removed in CH_2Cl_2, leaving behind a Ti triangle array (Figure 2a$_5$). Each Ti triangle in the array is uniform due to its firm adherence with the substrate. The Ti particles stack into a film rather than the particle distribution (see Supporting Information S2). Using the Ti triangle array as a base, we utilized atomic layer deposition technology to coat a 6.85-nm-thin layer of SnO_2 for an ensemble of TCAASs, and then obtained a gas sensor (Figure 2a$_6$).

Figure 2b-d show SEM images of the SnO_2 layer on the Ti triangle array, the Ti triangle array, and their template of the colloidal monolayer (with 1000 nm of the nanosphere diameter). In Figure 2d and the inset, a plane and a tilted view of the colloidal monolayer show that the 1000-nm-diameter nanospheres are closely arranged with a period of 1000 nm and triangular voice spaces. In Figure 2b and c, plane views of the SnO_2 layer (Figure 2b) and the triangle array (Figure 2c) depict their same alignment period between two sensor electrodes, whereas a comparison between their magnified views (the insets in Figure 2b and c) presents a thin coated layer of SnO_2 on the triangle array. For this SnO_2 layer, its average size of the crystallites is around 4 nm (see Supporting Information S3). More details about the XRD and the XPS characterizations, and SEM images related to using the other templates of colloidal monolayers (with 500, 750, and 2000 nm of nanosphere diameters) and further supporting the formation of the SnO_2 layer are respectively available in Supporting Information S3, S4, and S5.

By the colloidal-monolayer-based method, we use different colloidal monolayers (500, 750, 1000, and 2000 nm of the nanosphere diameters, see Supporting Information S4) to prepare triangle arrays (see Supporting Information S6 for their AFM images) and then coat with a 6.85-nm-thin layer of SnO_2. In Figure 2e-l, AFM images of the samples and their profile images describe the SnO_2 layers are of different values of inter-TCAAS spacing (i.e., *d*, the array period) versus the template nanosphere diameter (i.e., *D*): 289 nm/500 nm (Figure 2e and f), 433 nm/750 nm (Figure

2g and h), 577 nm/1000 nm (Figure 2i and j), and 1154 nm/2000 nm (Figure 2k and l). The above morphology metrics produce different roughness averages for the samples with different periods: 1.94 for the 289 nm, 1.59 for the 433 nm, 1.58 for the 577 nm, and 0.73 for the 1154 nm. These roughness averages indicate an order of the TCAAS size from large to small for the samples with different periods: the 289 nm > the 433 nm > the 577 nm > the 1154 nm.

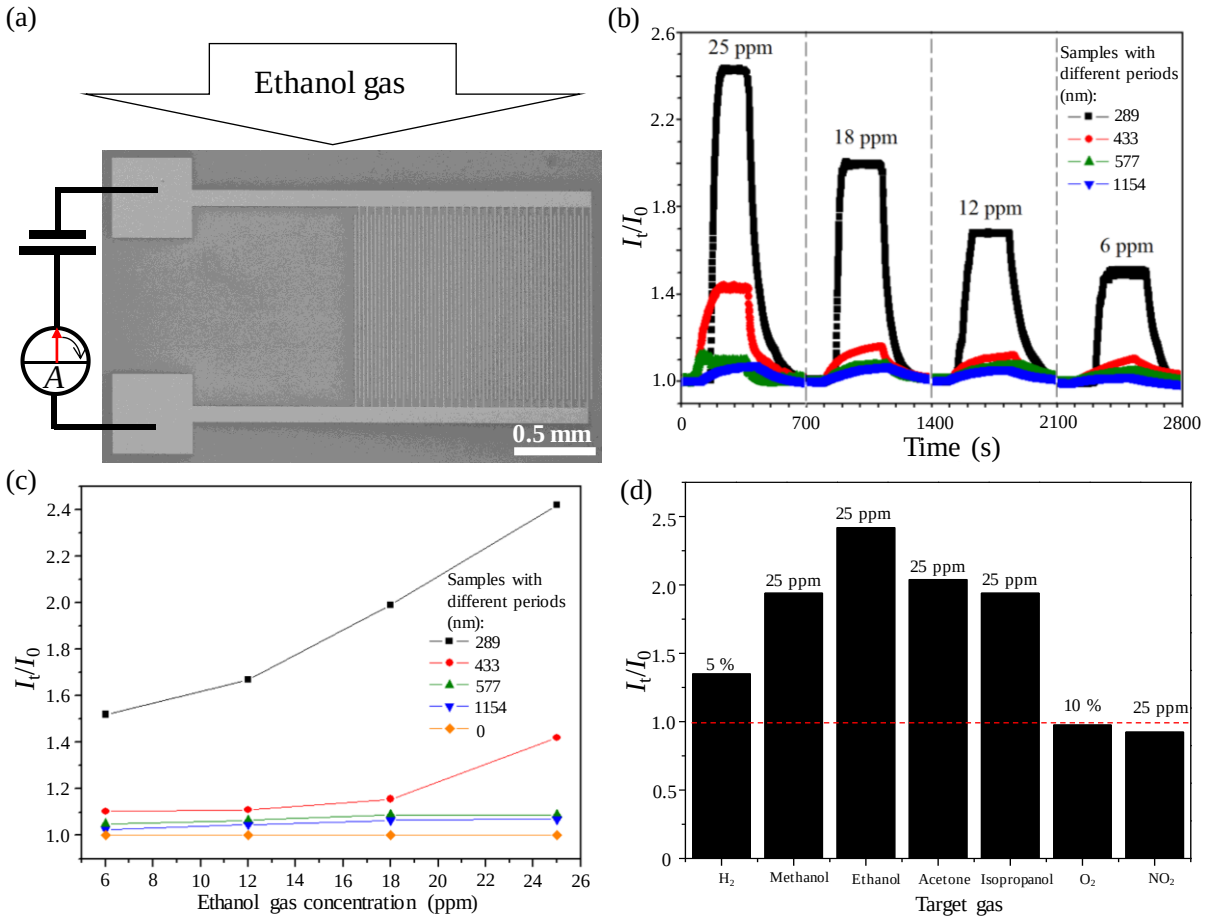

Figure 3. (a) Schematic illustration of the ethanol detection, and the SEM image showing the gas sensor device. (b) Gas-sensing responses to different concentrations of ethanol gases for different samples at room temperature. These samples are of different periods, such as 289, 433, 577, and 1154 nm. (c) The gas-sensing sensitivity (I_t/I_0) versus ethanol concentration (6, 12, 18 and 25 ppm) for the SnO_2 layers on different triangle arrays and the flat SnO_2 thin layer (i.e., the period is 0

nm). (d) Gas-sensing responses of the SnO_2-layer gas sensor (with a 289 nm period) to different target gases, including 5% H_2, 10% oxygen, 25 ppm of methanol, ethanol, acetone, and NO_2.

3.3. Gas-Sensing Properties of the Gas Sensors. SnO_2 samples with different TCAAS sizes are used as a gas sensor for detecting different concentrations of ethanol gases (25, 18, 12, and 6 ppm) at room temperature, as schematically illustrated in Figure 3a. Applied with a voltage of 4 V, the gas sensor sensitivity is defined as I_t/I_0.[36] I_0 and I_t are output currents of the sensor in air and the detecting atmosphere, respectively. Figure 3b presents gas-sensing responses to different concentrations of ethanol gases for the samples with periods of 289, 433, 577, and 1154 nm. It is found that the gas-sensing sensitivity increases with the increasing of the TCAAS size (i.e., the decreasing of periods). Shown by the sample with the largest TCAAS (289 nm of the period), the most sensitive gas-sensing is of the sensitivity (i.e., I_t/I_0) that can be up to 2.42, 1.99, 1.67, and 1.52 for 25, 18, 12, and 6 ppm of ethanol gases. This sensitive gas-sensing response indicates that this sample has a low detection limit of around 6 ppm ethanol gas or even the lower. Among the room-temperature SnO_2 gas sensors, the sensitivity of the 289 nm sample is also competitive. For example, in the room temperature detection of ethanol gas, the high sensitivity in the references is around 7 for 50 ppm ethanol,[37] which is closed to that of our sample (see Supporting Information Table S1).

In contrast, the sample with the smallest TCAAS (1154 nm of the period) is of a degraded sensitivity that is more than 2-times weaker than that of the largest TCAAS among detections of 6-25 ppm ethanol gases; even the ethanol gas is up to 25 ppm, the gas-sensing sensitivity of the sample with the 1154 nm period is just 1.08. Without TCAASs on an SnO_2 layer (i.e., the period is 0), the sample has no a gas-sensing response to the ethanol gas ranging from 6 ppm to 25 ppm, as depicted in Figure 3c. In Figure 3d, the investigation of gas-sensing selectivity confirms the

specific response of the sample (e.g., the 289-nm-period sample) to ethanol gas. In this work, the target gases include 5% H_2, 10% oxygen, and 25 ppm of methanol, ethanol, acetone, isopropanol, and NO_2. The sample sensitivity to the ethanol gas is higher than the others, and thus the ethanol gas is also selected as a model gas for the mechanism study. Note that the selectivity of our sample is fair as compared to those reported,[38-41] and a comparison shown in Table S2 suggests that this fair selectivity should be related to the low operated temperature (room temperature) and the low target gas concentration (25 ppm) in this work. Furthermore, in detecting 25 ppm ethanol gas at room temperature, our sensor also exhibits a stable response for (i) the humidity variation from 28% to 32% (ii) and a two-week measurement (see Supporting Information S7).

To investigate the mechanism of this TCAAS origin of gas-sensing, we firstly fabricate the samples into a field effect transistor and find an n-type conductance channel for all SnO_2 samples (see Supporting Information S8). By Hall effect measurements, the carrier density of the sample (n) is estimated around 2.3×10^{23} cm^{-3}. Introduced ethanol gaseous molecules can increase carrier density ($\Delta n > 0$) of these n-type samples to enhance their current intensity (characterized by $I_t/I_0 > 1$).[30] With the introduced 25 ppm ethanol gas, the current intensity increases 142%, 45%, 12%, and 8% for the samples with periods of 289, 433, 577, and 1154 nm (calculated by $\Delta I/I_0$, $\Delta I = I_t - I_0$). Given by the correlation between the current and the carrier density variation ($\Delta I = \Delta n A v Q$, A, v, and Q are respectively the cross-sectional area of conductor, carrier velocity, carrier charge), the carrier density increase is then estimated to 3.27×10^{23}, 1.04×10^{23}, 0.28×10^{23}, and 0.18×10^{23} for the samples with TCAAS from large to small. According to Equation 2, one introduced ethanol gaseous molecule can react with 3/4 adsorbed oxygen ion to increase 3/4 carrier for SnO_2. The adsorption quantity of ethanol gaseous molecules is then estimated to 4.35×10^{23}, 1.38×10^{23}, 0.37×10^{23}, 0.25×10^{23} for the sample with TCAAS from large to small. The estimated adsorption

quantity of ethanol gas on the large-TCAAS sample is distinctly higher than that of the small-TCAAS. Together with the TCAAS-dependent sensitivity, these results suggest that the high sensitivity manifested by the large-TCAAS sample should be attributed to its large adsorption quantity of the ethanol gas.

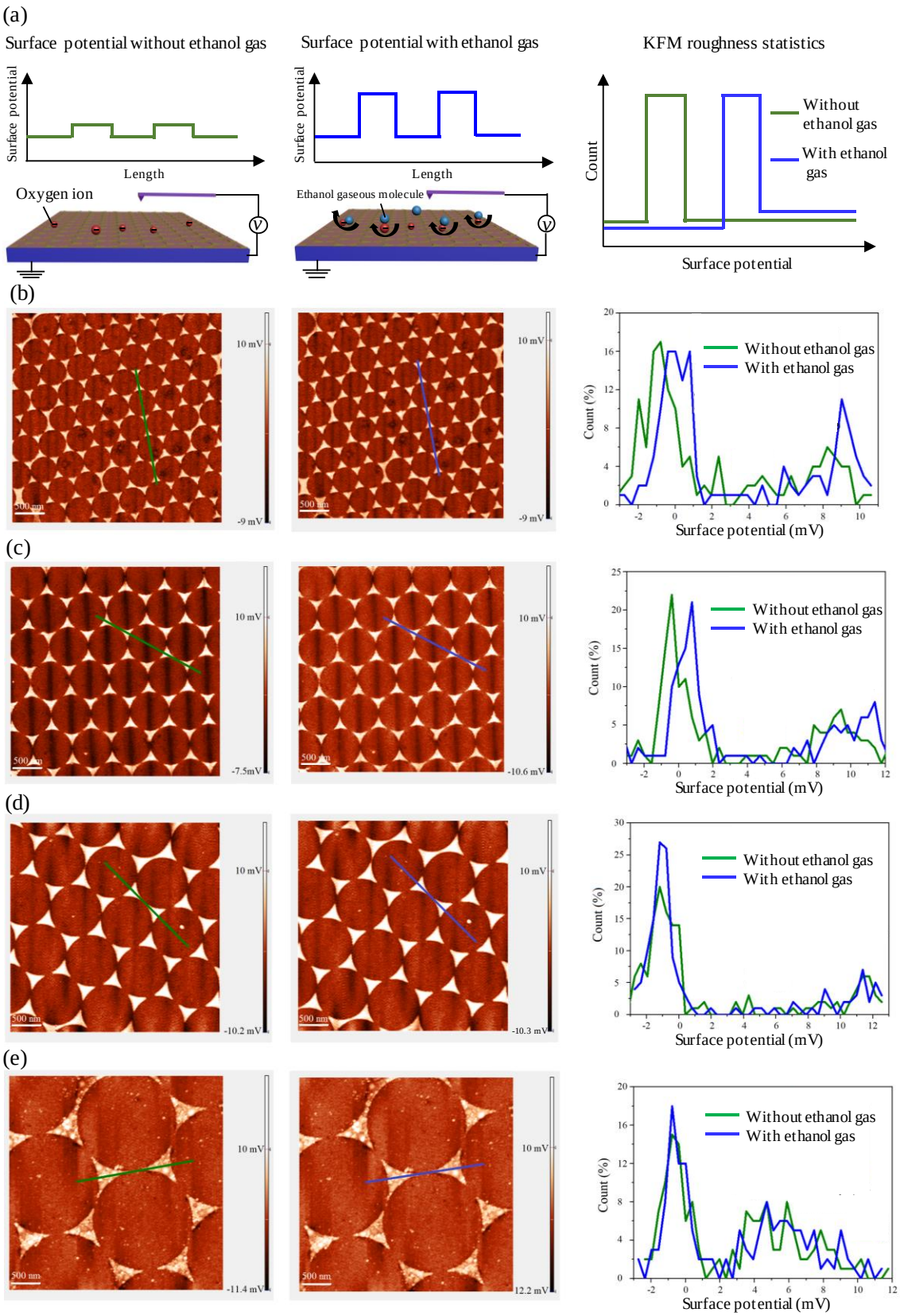
(a)
Surface potential without ethanol gas
Surface potential with ethanol gas
KFM roughness statistics
Surface potential
Length
Oxygen ion
Ethanol gaseous molecule
Count
Without ethanol gas
With ethanol gas
Surface potential
(b)
(c)
(d)
(e)
10 mV
-9 mV
-7.5mV
-10.6 mV
-10.2 mV
-10.3 mV
-11.4 mV
12.2 mV
500 nm
Count (%)
Surface potential (mV)

Figure 4. (a) Schematic representations showing the KFM setup for measuring a line-scanned surface potential across the samples with or without ethanol gas, and the KFM roughness statistics based on these two line-scanned surface potentials. Successive changes in atmospheres are made prior to each image acquisition: (i) in air and (ii) with 25 ppm ethanol, i.e., without and with ethanol gas. The right column shows KFM roughness statistics based on a line-scanned surface potential across a certain length of the samples. (b-e) KFM images of the samples with different periods, such as 289 nm (b), 433 nm (c), 577 nm (d) and 1154 nm (e).

3.4. Adsorption Enhancements on the Gas Sensors. To demonstrate the sample sensitivity is positively associated with its adsorption quantity of ethanol gas, we perform KFM characterizations on a 3.5 μm^2 area of each sample. Figure 4a schematically shows KFM setups, a line of the surface potential scanned across the samples, and the KFM roughness statistics based on the line-scanned surface potentials. Note that results of the KFM roughness statistics can show the percentages of different surface potential values. A positive and a negative shift of a surface-potential-percentage-dependent curve represent an increase and a decrease of surface potential, respectively. Next, according to the detecting atmosphere aforementioned, successive changes in the atmosphere are made prior to each KFM image acquisition: (i) in air and (ii) with 25 ppm ethanol (i.e., without and with ethanol gas). Figure 4b-e present the KFM images of the samples with periods of 289 nm (Figure 4b), 433 nm (Figure 4c), 577 nm (Figure 4d), and 1154 nm (Figure 4e), where the right column describes the KFM roughness statistics. It is found that, the samples with periods of 289 and 433 nm exhibit a distinctly positive shift of the curve. In contrast, an ambiguous shift is observed for the sample with periods of 577 and 1154 nm. This comparison reveals that a larger surface potential increase occurs on the samples with periods of 289 and 433 nm. In the case of surface potential average, the increase of surface potential average is up to

0.58 and 0.18 mV for the samples with periods of 289 and 433 nm, whereas the ambiguous increases of 0.06 and 0.005 mV respectively occur for the samples with periods of 577 and 1154 nm (see Table S3 in Supporting Information). Considering the fact that the surface potential of the SnO_2 can increase for the introduction of the ethanol gas, a larger surface-potential increase in the 289 nm and the 433 nm sample proves their higher adsorption quantity of the ethanol gas, where they possess a large TCAAS.

4. CONCLUSIONS

To summarize, this work offers a concept of adsorption active site for designing gas sensors with high sensitivity. According to the proposed concept, the fabrication process of the sensors is simple: by coating a 6.85-nm-thin SnO_2 on a triangle array, the SnO_2 gas sensor is prepared with an ensemble of triangular convex adsorption active sites (i.e., TCAASs). These adsorption active sites facilitate the surface adsorption of the sensor. In a room-temperature gas detection, the sensor exhibits a low detection limit of around 6 ppm ethanol gas. For investigating the gas-sensing mechanism, the samples with different TCAAS periods, ranging from 289 to 1154 nm, are also fabricated and present an adsorption-active-site-dependent sensitivity. Without adsorption active sites, the flat layer of SnO_2 has no responses even to 25 ppm ethanol gas. To reveal the mechanism of this adsorption-active-site-origin of sensitivity, we use KFM to investigate adsorption quantity of ethanol gas on the sample by its surface potential variation for ethanol gas. Importantly, the KFM results distinctly show an adsorption enhancement on the TCAAS by its large increase of surface potential after introducing ethanol gas. Based on the above, this work confirms that the creation of adsorption active sites can efficiently enhance surface adsorption for the sensitive gas-sensing. It is anticipated that the concept of the adsorption active site is applicable to different gas-sensing systems, serving as a general gas-sensing concept to design future gas sensors.

ASSOCIATED CONTENT

Supporting Information.

The Supporting Information is available free of charge.

The existence of ethanol gaseous molecules on the sample surface; the triangle bases of different materials; the transmission electron microscope, the XRD, and the XPS image of samples; SEM images of samples and their colloidal monolayer templates; the triangle base coated with different deposition cycles of SnO_2 in atomic layer deposition process; the AFM images of Ti triangle bases; the stability of the gas sensors; an n-type conductance channel of the gas sensors; the room temperature response of SnO_2 gas sensors to the reductive gases; the gas-sensing selectivity of the SnO_2 gas sensors; calculated adsorption quantities and surface-potential-average variations of the samples for introducing ethanol gas (PDF).

AUTHOR INFORMATION

Corresponding Author

* E-mail: yong.lei@tu-ilmenau.de.

ORCID

Yong Lei: 0000-0001-5048-7433

Notes

The authors declare no competing financial interest.

ACKNOWLEDGMENT

This work is financially supported by Federal Ministry of Education and Research in Germany (BMBF, ZIK-3DNanoDevice, 03Z1MN11), German Research Foundation (DFG: LE 2249_4-1 and LE 2249/5-1), and the China Scholarship Council.

REFERENCES

(1) Pan, X.; Liu, X.; Bermak, A.; Fan, Z. Self-Gating Effect Induced Large Performance Improvement of ZnO Nanocomb Gas Sensors. *ACS Nano* **2013**, *7*, 9318-9324.

(2) Cui, S.; Pu, H.; Wells, S.A.; Wen, Z.; Mao, S.; Chang, J.; Hersam, M.C.; Chen, J. Ultrahigh Sensitivity and Layer-Dependent Sensing Performance of Phosphorene-Based Gas Sensors. *Nat. Commun.* **2015**, *6*, 8632-8640.

(3) Cui, S.; Mao, S.; Lu, G.; Chen, J. Graphene Coupled with Nanocrystals: Opportunities and Challenges for Energy and Sensing Applications. *J. Phys. Chem. Lett.* **2013**, *4*, 2441-2454.

(4) Li, X.; Thai, M.L.; Dutta, R.K.; Qiao, S.; Chandran, G.T.; Penner, R.M. Sub-6 nm Palladium Nanoparticles for Faster, More Sensitive H_2 Detection Using Carbon Nanotube Ropes. *ACS Sensors* **2017**, *2*, 282-289.

(5) Koo, W.-T.; Qiao, S.; Ogata, A.F.; Jha, G.; Jang, J.-S.; Chen, V.T.; Kim, I.-D.; Penner, R.M. Accelerating Palladium Nanowire H_2 Sensors Using Engineered Nanofiltration. *ACS Nano* **2017**, *11*, 9276-9285.

(6) Ellis, J.E.; Green, U.; Sorescu, D.C.; Zhao, Y.; Star, A. Indium Oxide—Single-Walled Carbon Nanotube Composite for Ethanol Sensing at Room Temperature. *J. Phys. Chem. Lett.* **2015**, *6*, 712-717.

(7) Huang, W.; Zhuang, X.; Melkonyan, F.S.; Wang, B.; Zeng, L.; Wang, G.; Han, S.; Bedzyk, M.J.; Yu, J.; Marks, T.J.; Facchetti, A. UV-Ozone Interfacial Modification in Organic Transistors for High-Sensitivity NO_2 Detection. *Adv. Mater.* **2017**, *29*, 1701706-1701716.

(8) Wang, H.; Dou, K.; Teoh, W.Y.; Zhan, Y.; Hung, T.F.; Zhang, F.; Xu, J.; Zhang, R.; Rogach, A.L. Engineering of Facets, Band Structure, and Gas-Sensing Properties of Hierarchical Sn^{2+}-Doped SnO_2 Nanostructures. *Adv. Funct. Mater.* **2013**, *23*, 4847-4853.

(9) Xu, S.P.; Sun, F.Q.; Gu, F.; Zuo, Y.; Zhang, L.; Fan, C.; Yang, S.; Li, W. Photochemistry-Based Method for the Fabrication of SnO_2 Monolayer Ordered Porous Films with Size-Tunable Surface Pores for Direct Application in Resistive-Type Gas Sensor. *ACS Appl. Mater. Interfaces* **2014**, *6*, 1251-1257.

(10) Zhou, Z.-Y.; Tian, N.; Li, J.-T.; Broadwell, I.; Sun, S.-G. Nanomaterials of High Surface Energy with Exceptional Properties in Catalysis and Energy Storage. *Chem. Soc. Rev.* **2011**, *40*, 4167-4185.

(11) Gurlo, A. Nanosensors: Towards Morphological Control of Gas Sensing Activity. SnO_2, In_2O_3, ZnO and WO_3 Case Studies. *Nanoscale* **2011**, *3*, 154-165.

(12) Kuang, Q.; Wang, X.; Jiang, Z.; Xie, Z.; Zheng, L. High-Energy-Surface Engineered Metal Oxide Micro- and Nanocrystallites and Their Applications. *Acc. Chem. Res.* **2014**, *47*, 308-318.

(13) Wu, J.; Feng, S.; Wei, X.; Shen, J.; Lu, W.; Shi, H.; Tao, K.; Lu, S.; Sun, T.; Yu, L.; Du, C.; Miao, J.; Norford, L.K. Facile Synthesis of 3D Graphene Flowers for Ultrasensitive and Highly Reversible Gas Sensing. *Adv. Funct. Mater.* **2016**, *26*, 7462-7469.

(14) Kreno, L.E.; Hupp, J.T.; Duyne, R.P.V. Metal-Organic Framework Thin Film for Enhanced Localized Surface Plasmon Resonance Gas Sensing. *Anal. Chem.* **2010**, *82*, 8042-8046.

(15) Wang, J.X.; Sun, X.W.; Xie, S.S.; Yang, Y.; Chen, H.Y.; Lo, G.Q.; Kwong, D.L. Preferential Growth of SnO_2 Triangular Nanoparticles on ZnO Nanobelts. *J. Phys. Chem. C* **2007**, *111*, 7671-7675.

(16) Ma, W.; Yang, H.; Wang, W.; Gao, P.; Yao, J. Ethanol Vapor Sensing Properties of Triangular Silver Nanostructures Based on Localized Surface Plasmon Resonance. *Sensors* **2011**, *11*, 8643-8653.

(17) Liu, N.; Tang, M.L.; Hentschel, M.; Giessen, H.; Alivisatos, A.P. Nanoantenna-Enhanced Gas Sensing in a Single Tailored Nanofocus. *Nat. Mater.* **2011**, *10*, 631-636.

(18) Yang, S.K.; Lapsley, M.I.; Cao, B.Q.; Zhao, C.L.; Zhao, Y.H.; Hao, Q.Z.; Kiraly, B.; Scott, J.; Li, W.Z.; Wang, L.; Lei, Y.; Huang, T.J. Large-Scale Fabrication of Three-Dimensional Surface Patterns Using Template-Defined Electrochemical Deposition. *Adv. Funct. Mater.* **2013**, *23*, 720-730.

(19) Morarescu, R.; Shen, H.; Vallée, R.A.L.; Maes, B.; Kolaric, B.; Damman, P. Exploiting the Localized Surface Plasmon Modes in Gold Triangular Nanoparticles for Sensing Applications. *J. Mater. Chem.* **2012**, *22*, 11537-11542.

(20) Haes, A.J.; Zou, S.; Schatz, G.C.; Duyne, R.P.V. Nanoscale Optical Biosensor: Short Range Distance Dependence of the Localized Surface Plasmon Resonance of Noble Metal Nanoparticles. *J. Phys. Chem. B* **2004**, *108*, 6961-6968.

(21) Haes, A.J.; Zou, S.; Schatz, G.C.; Duyne, R.P.V. A Nanoscale Optical Biosensor: The Long Range Distance Dependence of the Localized Surface Plasmon Resonance of Noble Metal Nanoparticles. *J. Phys. Chem. B* **2004**, *108*, 109-116.

(22) Haes, A.J.; Chang, L.; Klein, W.L.; Duyne, R.P.V. Detection of a Biomarker for Alzheimer's Disease from Synthetic and Clinical Samples Using a Nanoscale Optical Biosensor. *J. Am. Chem. Soc.* **2005**, *127*, 2264-2271.

(23) Chen, W.; Cai, W.P.; Lei, Y.; Zhang, L.D. A Sonochemical Approach to the Confined Synthesis of Palladium Nanocrystalline within Mesoporous Silica, *Mater. Lett.* **2001**, *50*, 53-56.

(24) Wang, S.X.; Wang, M.T.; Lei, Y.; Zhang, L.D. Anchor Effect in Poly (Styrene Maleic Anhydride)/TiO_2 Nanocomposites. *J. Mater. Sci. Lett.* **1999**, *18*, 2009-2012.

(25) Kolmakov, A.; Potluri, S.; Barinov, A.; Mentes, T.O.; Gregoratti, L.; Nino, M.A.; Locatelli, A.; Kiskinova, M. Spectromicroscopy for Addressing the Surface and Electron Transport Properties of Individual 1-D Nanostructures and Their Networks. *ACS Nano* **2008**, *2*, 1993-2000.

(26) Xu, S.P.; Zhao, H.P.; Xu, Y.; Xu, R.; Lei, Y. Carrier Mobility-Dominated Gas Sensing: A Room-Temperature Gas-Sensing Mode for SnO_2 Nanorod Array Sensors. *ACS Appl. Mater. Interfaces* **2018**, *10*, 13895-13902.

(27) Tricoli, A.; Righettoni, M.; Teleki, A. Semiconductor Gas Sensors: Dry Synthesis and Application. *Angew. Chem. Int. Ed.* **2010**, *49*, 7632-7659.

(28) Hall, G.K.; Mee, C.H.B. The Surface Potential of Oxygen on Iron, Cobalt and Manganese. *Surf. Sci.* **1971**, *28*, 598-606.

(29) Libre, J.M.; Barbaux, Y.; Grzybowska, B.; Bonnelle, J.P. A Surface Potential Study of Adsorbed Oxygen Species on a $Bi_2Mo_3O_{12}$ Catalyst. *React. Kinet. Catal. Lett.* **1982**, *20*, 249-254.

(30) Ogawa, H.; Nishikawa, M.; Abe, A. Hall Measurement Studies and an Electrical Conduction Model of Tin Oxide Ultrafine Particle Films. *J. Appl. Phys.* **1982**, *53*, 4448-4455.

(31) Gouveia, R.F.; Galembeck, F. Electrostatic Charging of Hydrophilic Particles Due to Water Adsorption. *J. Am. Chem. Soc.* **2009**, *131*, 11381-11386.

(32) Gouveia, R.F.; Bernardes, J.S.; Ducati, T.R.D.; Galembeck, F. Acid–Base Site Detection and Mapping on Solid Surfaces by Kelvin Force Microscopy (KFM). *Anal. Chem.* **2012**, *84*, 10191-10198.

(33) Moutet, P.; Deram, P.; Sangeetha, N.M.; Ressier, L. Dynamics of Dielectrophoretic-Force-Directed Assembly of $NaYF_4$ Colloidal Nanocrystals into Tunable Multilayered Micropatterns. *J. Phys. Chem. Lett.* **2014**, *5*, 2988-2993.

(34) Melitz, W.; Shen, J.; Kummel, A.C.; Lee, S. Kelvin Probe Force Microscopy and Its Application. *Surf. Sci. Rep.* **2011**, *66*, 1-27.

(35) Sun, F.Q.; Cai, W.; Li, Y.; Jia, L.; Lu, F. Direct Growth of Mono- and Multilayer Nanostructured Porous Films on Curved Surfaces and Their Application as Gas Sensors. *Adv. Mater.* **2005**, *17*, 2872-2877.

(36) Wang, Y.-T.; Whang, W.-T.; Chen, C.-H. Hollow V_2O_5 Nanoassemblies for High-Performance Room-Temperature Hydrogen Sensors. *ACS Appl. Mater. Interfaces* **2015**, *7*, 8480-8487.

(37) Zhao, Q.; Gao, Y.; Bai, X.; Wu, C.; Xie, Y. Facile Synthesis of SnO_2 Hollow Nanospheres and Applications in Gas Sensors and Electrocatalysts. *Eur. J. Inorg. Chem.* **2006**, *2006*, 1643-1648.

(38) Fan, X.-X.; He, X.-L.; Li, J.-P.; Gao, X.-G.; Jia, J. Ethanol Sensing Properties of Hierarchical SnO_2 Fibers Fabricated with Electrospun Polyvinylpyrrolidone Template. *Vacuum* **2016**, *128*, 112-117.

(39) Cheng, L.; Ma, S.Y.; Wang, T.T.; Li, X.B.; Luo, J.; Li, W.Q.; Mao, Y.Z.; GZ, D.J. Synthesis and Characterization of SnO_2 Hollow Nanofibers by Electrospinning for Ethanol Sensing Properties. *Mater. Lett.* **2014**, *131*, 23-26.

(40) Zong, Y.; Cao, Y.L.; Jia, D.Z.; Hu, P.F. The Enhanced Gas Sensing Behavior of Porous Nanocrystalline SnO_2 Prepared by Solid-State Chemical Reaction. *Sens. Actuator, B* **2010**, *145*, 84-88.

(41) Sun, P.; Mei, X.D.; Cai, Y.X.; Ma, J.; Sun, Y.F.; Liang, X.S.; Liu, F.M.; Lu, G.Y. Synthesis and Gas Sensing Properties of Hierarchical SnO_2 Nanostructures. *Sens. Actuator, B* **2013**, *187*, 301-307.